Carbon 197 (2022) 253–263

Contents lists available at ScienceDirect

Carbon

journal homepage: www.elsevier.com/locate/carbon

Laser-induced graphene from paper for non-enzymatic uric acid electrochemical sensing in urine

Bohdan Kulyk [a,b], Sónia O. Pereira [a], António J.S. Fernandes [a], Elvira Fortunato [b], Florinda M. Costa [a,*], Nuno F. Santos [a,**]

[a] i3N – Department of Physics, University of Aveiro, Campus Universitário de Santiago, Aveiro, 3810-193, Portugal
[b] i3N/CENIMAT, Department of Materials Science and CEMOP/UNINOVA, NOVA School of Science and Technology, NOVA University Lisbon, Campus de Caparica, Caparica, 2829-516, Portugal

ARTICLE INFO

Keywords:
Graphene
Paper-LIG
Uric acid
Human urine
Electrochemical biosensors
Flexible electronics

ABSTRACT

Laser-induced graphene from paper (paper-LIG) was applied in non-enzymatic electrochemical sensing of uric acid (UA) in human urine. Paper-LIG was formed by CO_2 laser modification of paper into a 3D graphene arrangement. Kinetic analysis of paper-LIG electrodes returned effective heterogeneous electron transfer standard rate constants of 1.4×10^{-3} cm s^{-1} and 7.8×10^{-4} cm s^{-1} for $[Ru(NH_3)_6]^{2+/3+}$ and $[Fe(CN)_6]^{4-/3-}$ redox probes, respectively. These electrodes were able to detect and quantify uric acid in PBS within the 10–300 μM range at pH between 5.6 and 7.4. At pH 7.4, a linear response ($R^2 = 0.999$) from 10 to 250 μM was achieved, with a limit of detection of 3.97 μM and a sensitivity of 0.363 μA cm^{-2} μM^{-1}. Paper-LIG electrodes denoted adequate selectivity in synthetic urine as well as in ascorbic acid (AA) and dopamine (DA)-containing electrolytes. Determination of urinary UA content in human samples returned a concentration of c.a. 1.8–1.9 mM, within the range for healthy individuals. Recoveries of samples spiked with 50 and 100 μM UA were 100.6% and 95.4%, respectively, with satisfactory reproducibility and stability. These cheap, lightweight, flexible, and eco-friendly paper-LIG biosensors for non-enzymatic quantification of UA in human urine pave the way to widespread application in the detection of other important biomarkers.

1. Introduction

The unique combination of outstanding properties of graphene, a two-dimensional sheet of carbon atoms first isolated in 2004 [1], has spurred a considerable body of work aimed at realizing the substantial promise it holds in a vast number of fields [2]. Among these, the advancements in its potential biomedical applications are particularly encouraging, encompassing topics such as drug delivery [3,4], tissue engineering [5], and biosensors [6]. In the latter, and particularly in the context of electrochemical sensing, graphene and graphene-based materials are excellent candidates on account of their electrocatalytic activity and electrochemical performance [7,8]. With heterogeneous electron transfer (HET) rates rivaling or even exceeding those of other commonly employed materials such as glassy carbon [9], graphite [10] and carbon nanotubes [9], while aided by its high specific surface area and chemical stability, graphene has a bright future as an electrochemical transducer [11].

Adding to an already rich tapestry of graphene-based materials, in 2014 it was shown that irradiation of flexible commercial polymers such as polyimide with an infrared (CO_2) laser can produce a porous, conductive graphene foam [12]. This material was dubbed laser-induced graphene (LIG), and the ability to easily pattern conductive paths and electrodes onto flexible substrates opened the door to its use in actuators [13], sensors [14–19], and energy storage devices [12], among other applications. Currently, LIG can be formed using different laser wavelengths [14,19], and on different carbon-containing substrates, including nature-derived materials such as wood [20], cork [21], xylan [22], and paper (the latter referred to as paper-LIG) [23].

Paper is a remarkable material in its own right. Being cheap, lightweight, and flexible, it finds many uses in the daily lives of people throughout the world [24]. In addition to that, paper is recyclable and biodegradable, features which are worth noting as humanity faces considerable challenges concerning the management of natural resources and the preservation of the environment [25].

* Corresponding author.
** Corresponding author.
E-mail addresses: flor@ua.pt (F.M. Costa), nfsantos@ua.pt (N.F. Santos).

https://doi.org/10.1016/j.carbon.2022.06.013
Received 29 March 2022; Received in revised form 27 May 2022; Accepted 8 June 2022
Available online 15 June 2022

These attributes make paper particularly well suited for application in low-cost point-of-care biomedical devices [26]. This has been best exploited in lateral flow tests [27], and currently there is a growing interest concerning paper-based microfluidic assay devices (μPADs) [28], taking advantage of paper's water absorption capacity and wicking ability. Being cheap and disposable, these devices seek to facilitate the access to affordable and fast on-site diagnostics and healthcare. Graphene-based materials have also been employed in paper-based analytical devices [29–33]. However, as most of the examples of paper-supported graphene biosensors require a specific step for the application of the graphene-based material onto the paper, none of them can boast the ease of fabrication characteristic of paper-LIG, where the paper itself is converted into the electrochemically active graphene material. Even comparing to the previously reported biosensors employing polyimide derived LIG (PI-LIG), the abundance and availability of paper at a substantially lower cost presents a considerable advantage from the production point of view. Recognizing these benefits relative to LIG obtained from synthetic polymers, recently paper-LIG started getting attention in the detection of analytes such as ascorbic and caffeic acids [34], and more recently in enzymatic amperometric biosensors for glucose detection [35], but so far sensing in real biological samples has not been demonstrated using this material.

In this work, we employ laser-induced graphene obtained from common filter paper as an electrode for the non-enzymatic electrochemical detection and quantification of uric acid (UA). Uric acid is the main product of purine metabolism, constituting a clinically relevant compound, since abnormal levels of UA are associated to diseases such as hyperuricemia, gout, inflammatory arthritis, and chronic renal disease. In conjunction with other biomarkers, UA concentration levels are also useful for the screening and monitoring of some cardiovascular diseases and diabetes-related complications [36,37].The sensing capabilities of these paper-LIG electrodes are demonstrated both in artificial and real human urine samples. Both the synthesis of paper-LIG and the electrochemical measurements are facile and fast, while the sensors themselves are low-cost and disposable, encouraging real-life applications in affordable, environmentally friendly biosensing.

2. Material and methods

2.1. Reagents and electrolyte solutions

Whatman grade 40 hardened ashless cellulose filter paper (95 g m^{-2}, 210 μm of thickness, ≤0.007% ash content) was obtained from Cytiva. A commercial phosphate based Anti-Flame fire retardant was purchased from BBT. Electrodag 1415 silver paste and Lacomit varnish G371 were acquired from Agar Scientific.

Hexaaminеruthenium(III) chloride ($[Ru(NH_3)_6]Cl_3$, >98%), sodium sulphate (Na_2SO_4, ACS reagent, ≥99.0% anhydrous, powder), sodium citrate tribasic dihydrate ($Na_3C_6H_5O_7.2H_2O$, ACS reagent, ≥ 99.0%), creatinine ($C_4H_7N_3O$, anhydrous, ≥98%), urea (CH_4N_2O, ReagentPlus®, ≥99.5%, pellets), potassium chloride (KCl, SigmaUltra Minimum 99.0%), sodium chloride (NaCl, ACS reagent, ≥ 99.0%), ammonium chloride (NH_4Cl, ACS reagent, ≥ 99.5%), potassium oxalate monohydrate ($K_2C_2O_4.H_2O$, ACS reagent, 99%), magnesium sulphate heptahydrate ($MgSO_4.7H_2O$, ReagentPlus®, ≥99.0%), sodium phosphate monobasic monohydrate ($NaH_2PO_4.H_2O$, ACS reagent, ≥ 98%), and sodium phosphate dibasic heptahydrate ($Na_2HPO_4.7H_2O$, ≥ 99.99% trace metals basis) were purchased from Sigma-Aldrich. Potassium hexacyanoferrate(II) trihydrate ($K_4[Fe(CN)_6].3H_2O$, AGR) was supplied by Labkem. Uric acid ($C_5H_4N_4O_3$, 99%), dopamine hydrochloride (>99%) and ascorbic acid (>99.7%) were obtained from Alfa Aesar. Calcium chloride ($CaCl_2$, anhydrous granules) was acquired from Supelco, Merck. Deionized (DI) water was obtained from a MilliQ water purification system, with a resistivity of 18.2 MΩ cm. All reagents were used as received.

Phosphate buffer saline (PBS) solution at pH 7.4 was prepared using tablets from Fisher Bioreagents, 1 tablet per 200 mL providing a solution with 0.137 M NaCl, 0.027 M KCl and 10 mM of phosphate buffer. The phosphate buffer saline solutions, with pH 6.6 and 5.6, were prepared keeping constant the phosphate buffer concentration in 10 mM and the ionic strength (0.137 M NaCl and 0.027 M KCl). Ratios of 6:4 mM and 9.5:0.5 mM of NaH_2PO_4:Na_2HPO_4 were used to prepare the pH 6.6 and 5.6, respectively. The pH of each solution was confirmed using a pH meter form Hanna Instruments.

Synthetic Urine (SU) was prepared a day prior to its use, as described in Ref. [38]. Briefly, the compounds that composed the urine were weighted and added in the following order to 1 L of deionized (DI) water, at 37 °C under stirring: 1.700 g Na_2SO_4, 0.720 g sodium citrate, 0.881 g creatinine, 15 g urea, 2.308 g KCl, 1.756 g NaCl, 0.185 g $CaCl_2$, 1.266 g NH_4Cl, 0.035 g potassium oxalate, 1.082 g $MgSO_4.7H_2O$, 2.912 g $NaH_2PO_4.H_2O$ and 0.831 g $Na_2HPO_4.7H_2O$. After overnight stirring at 37 °C, a pH value of 6.0 was measured with the pH meter. Uric acid was not added in this formulation of SU, as it is the compound under analysis throughout this work.

Real human urine sample was voluntarily provided by one of the co-authors, a healthy male aged between 30 and 40 years (being fully aware and consenting of all the implications of the present study, in accordance with all the ethical requirements). The volunteer collected the first morning urine sample after fasting for at least 8 h and the urine was immediately stored at 4 °C and measured within 2 h from collection, with no requirement for long-term sample storage and having been properly disposed of immediately after the measurement. In accordance with the literature [38], first morning and fasting urine samples do not have contaminants from the food consumed by the person, and thus the represent the urine composition due to metabolism only.

2.2. Paper-LIG electrode fabrication

The cellulose filter paper was sprayed with the fire retardant and left to dry in air. It was then irradiated by a K40 CO_2 (10.6 μm) continuous wave 40 W laser engraver, by Liaocheng Julong CO. Ltd., operated in a unidirectional line scan mode, at 800–900 mW of power, 30 mm s^{-1} of scan speed, and with a line separation of 0.1 mm. Two irradiation steps were employed, the first one at 9 mm below focus and the second one at focus. A rectangular area of 20 × 5 mm^2 was irradiated for each electrode, transforming the paper into paper-LIG, and later cut out with a 2.5 mm margin on each side of this area. It should be noted that care must be taken during the LIG production regarding possible laser power fluctuations and unintentional defocusing of the laser beam. For this reason, laser power was closely monitored between the irradiation steps. Moreover, some cracks can appear during paper-LIG production due to power fluctuations, and preliminary quality check and electrode selection procedure is necessary. All these factors can severely affect the paper-LIG electroanalytical performance and thus the reproducibility of the sensors.

The electrodes were then rinsed with 150 mL of DI water to wash off the excess fire retardant and left to dry overnight in air. Next, a 20 awg tin-coated copper wire was attached at the end of the irradiated area, using silver paste. Finally, non-conductive and electrochemically inactive Lacomit varnish was used to encapsulate the electrode (on both sides of the paper) and the contact wire, leaving exposed a ~5 × 5 mm^2 area of paper-LIG to act as the active area.

2.3. Morphological and structural analysis

Secondary electron scanning electron microscopy (SE−SEM and BSE-SEM) images were acquired using a Vega 3 SBH system, by TESCAN, with an acceleration voltage of 15 kV and a working distance of 15 mm. Raman spectroscopy was performed using a Jobin Yvon HR800 Raman system, by Horiba, and a He–Cd 441.6 nm laser, by Kimmon, with a ×50 lens (NA = 0.5), by Olympus. A neutral density filter OD = 1 was used to attenuate the laser power to prevent any potential thermally

induced chemical modification of the samples. Sheet resistance measurements were performed by the van der Pauw method, using a Keysight B2902A dual-channel source meter unit. XPS spectra were acquired in an Axis Supra Spectrometer by Kratos Analytical using monochromatized Al Ka radiation at an X-ray power of 225 W. The pass energy was 80 eV for survey scans and 5 eV for detailed scans. The XPS spectrum of paper was corrected by taking the C–C/C–H peak as reference (284.8 eV). All the fittings were performed with CasaXPS Version 2.3.19PR1.0. The samples were washed with DI water before the measurements.

2.4. Electrochemical methods and apparatus

A Versastat3 (Princeton Applied Research) was used for all the electrochemical measurements. A homemade 3D-printed electrochemical cell was employed in the three-electrode configuration, where paper-LIG was the working electrode (WE), a standard Calomel electrode (SCE) was the reference electrode (RE), placed at a distance from the WE of twice the diameter of the SCE tip, and a Pt wire was the counter electrode (CE). The measurements were performed at high electrolyte volume to electrode area ratio conditions (25 mm^2 WE area in 35 mL electrolyte solution). In order to stabilize the electrodes, ten potential cycles between −1 and 1 V vs. SCE at a scan rate of 100 mV s^{-1}, starting and stopping at the open circuit potential, were performed in PBS electrolyte prior to any measurements (Fig. S1). The EIS measurements were performed employing a sinusoidal 5 mV perturbation at the open circuit potential (223 mV vs. SCE), within the 1 kHz to 0.1 Hz range.

The Nicholson method was employed to estimate the effective heterogeneous electron transfer standard rate constant of paper-LIG electrode k^0_{eff}, using both reversible outer-sphere ($[Ru(NH_3)_6]^{3+}$) and inner-sphere ($[FeCN_6]^{4-}$) redox probes. Briefly, a collection of values for a kinetic parameter Ψ was retrieved via the scan rate (ν)-dependent cyclic voltammograms through

$$\Psi = \frac{-0.6288 + 0.0021\Delta E_p}{1 - 0.017\Delta E_p}, \quad (1)$$

where ΔE_p is the separation of the anodic and cathodic peak potentials for each scan rate. If the electrode reaction proceeds in a quasi-reversible regime, i.e. for ΔE_p up to about 250 mV, and assuming (i) a similar diffusion coefficient D for the oxidized and reduced forms in aqueous solution (9.10×10^{-6} cm^2 s^{-1} and 6.67×10^{-6} cm^2 s^{-1} for $[Ru(NH_3)_6]^{3+/2+}$ and $[Fe(CN)_6]^{4-/3-}$, respectively), and (ii) symmetrical redox kinetics of the redox couple (charge transfer coefficient of 0.5), one can infer k^0_{eff} (cm s^{-1}) by

$$\Psi = \frac{k^0_{eff}}{\left(\frac{n\pi FD\nu}{RT}\right)^{\frac{1}{2}}}, \quad (2)$$

where $n = 1$ is the number of electrons involved in the $[Ru(NH_3)_6]^{2+/3+}$ and $[Fe(CN)_6]^{4-/3-}$ redox reaction, F is the Faraday constant (96485.33 C mol^{-1}), R the universal gas constant (8.314 J mol^{-1} K^{-1}) and T the absolute temperature (K). The electrolyte solution was thoroughly bubbled with N_2 for 60 min and kept under N_2 blanket during these measurements, as to eliminate the interfering contribution from the oxygen reduction reaction occurring at about −0.5 V vs. SCE. Voltammograms for HET estimations were acquired from faster to slower scan rates.

Differential pulse voltammetry (DPV) was employed for UA sensing tests via oxidation signal. The DPV parameters were chosen based on previous optimization for the paper-LIG electrodes: pulse height was 45 mV, pulse width 0.03 s, step height 3 mV and step width 0.3 s, yielding a scan rate of 10 mV s^{-1}. All measurements were performed in quadruplicate with increasing concentration of UA. The electrodes were washed with DI water in between each measurement in UA-containing samples to remove adsorbed reactants/products at the electrode's surface.

3. Results and discussion

3.1. Synthesis and characterization of paper-LIG

Cellulose paper was used for the synthesis of laser-induced graphene. While non-enzymatic uric acid sensors based on PI-LIG have been reported previously, cellulose paper presents considerable advantages as the precursor substrate, from both the production and the application standpoints. Specifically, paper is substantially cheaper and more widely available than the commercial polymers used for LIG synthesis. Moreover, paper is recyclable and biodegradable. These attributes make paper-LIG biosensors extremely attractive for low-cost, single-use, point-of-care analytical applications, particularly in low-income areas. For the synthesis, illustrated in Fig. 1a, the cellulose paper is treated with an environmentally friendly fire retardant to prevent its breakdown into volatile compounds [23]. Then, the paper is irradiated twice with a 10.6 μm laser, first out of focus and then in focus. The first irradiation promotes the conversion of cellulose into char, while the second one graphitizes it into laser-induced graphene [15]. The resulting material presents Raman spectra characteristic of LIG, with well defined, symmetrical D, G and 2D peaks (Fig. 1b) [12]. The magnitude of the I_D/I_G intensity ratio is closely related to structural disorder in the sp^2 carbon lattice, scaling with the concentration of defects [39]. Paper-LIG displays an I_D/I_G ratio close to 1 for 442 nm excitation wavelength, which outlines a relatively high concentration of defects. Provided that it does not compromise the electrical conductivity, this is desirable for electrochemical sensing, since defects in carbon nanostructures, such as edge plane defects, are known to play an important role in electron transfer due to enhanced local density-of-states [40,41]. A further inspection of these flexible paper-LIG electrodes, depicted in Fig. 1c after the encapsulation with insulating varnish, allows to compare the morphology of paper before (Fig. 1d and e) and after (Fig. 1f–h) its transformation into LIG, as revealed by secondary electron scanning electron microscopy (SE−SEM). Here, it can be seen that the irradiated cellulose fibers become porous, forming web-like structures. Similar porosity formation is known to occur in phosphoric acid activation of cellulosic material (paper, wood, etc.) to obtain activated carbon, where cross-links are formed through phosphate linkages [42,43], which is relevant here due to the use of the phosphate based fire retardant. This porosity, which can be associated with a larger surface area, can be particularly beneficial for biosensing applications.

Additional information about the transformation of paper into paper-LIG can be obtained from XPS analysis. Fig. 1i shows overview spectra of fire retardant treated paper and the resulting paper-LIG (both after being washed with DI water). While the paper substrate shows the presence of only C and O, characteristic of cellulose, after laser irradiation one finds additional chemical elements, namely P, N and Na. This is due to some retention of the phosphate-based fire retardant in the paper-LIG, most likely inside the porous structure that is formed. As for the C 1s peak (Fig. 1j), in the case of paper the most prominent components are due to C–O and C═O bonds, at 286.46 eV and 287.91 eV, respectively, accompanied by less intense components at 284.80 eV and 289.32 eV, assigned to C–C/C–H and O–C═O bonds [44]. For paper-LIG, on the other hand, the main feature is the asymmetrical component at 284.36 eV, corresponding to sp^2-hybridized carbon, while the components corresponding to carbons bonded with oxygen [45] are far less prominent than in non-irradiated paper. The relative atomic concentration of C–O bonds, for example, decreases from 69.69% to 8.92% after laser irradiation. This points toward the release of oxygen under laser irradiation, accompanied by the reorganization of the carbon atoms to form graphitic domains (although some oxygen remains, either due to some unconverted cellulose or due to partial oxidation of the paper-LIG). The predominantly sp^2 nature of paper-LIG is further confirmed by the

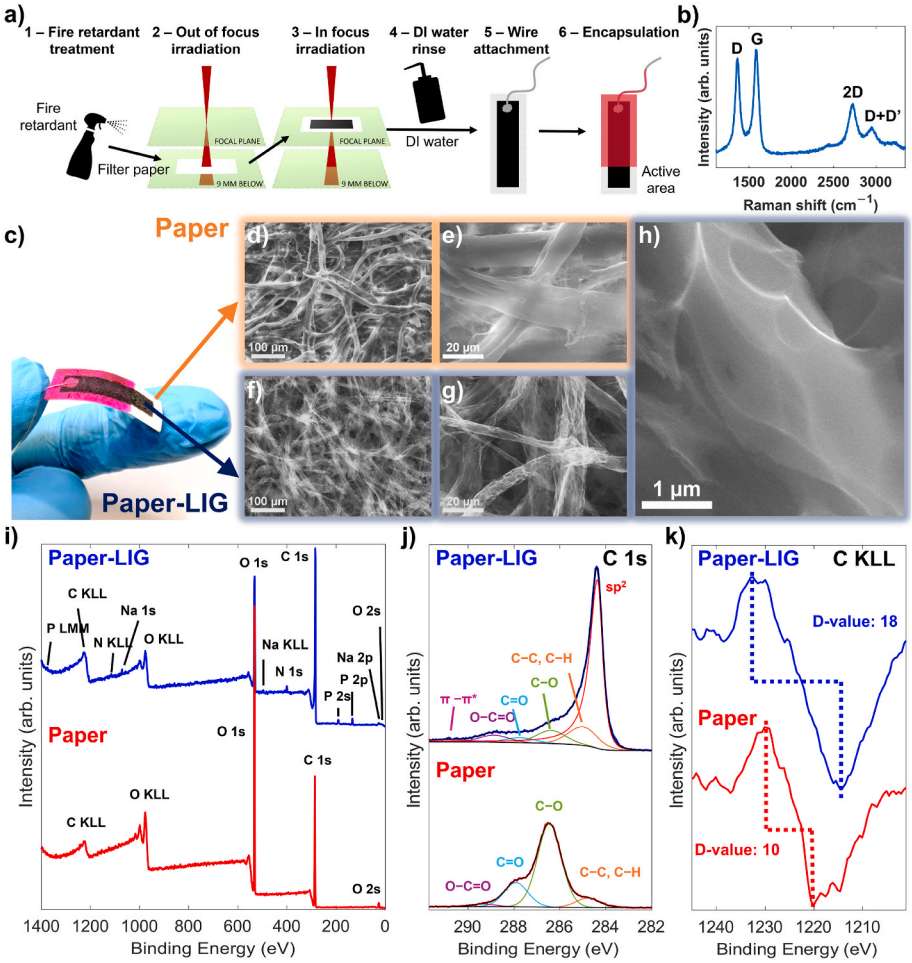

Fig. 1. Synthesis and characterization of paper-LIG. **(a)** Schematic illustration of the preparation of the paper-LIG electrodes. **(b)** Representative Raman spectrum of paper-LIG. **(c)** Photograph of a paper-LIG sensing unit. SEM micrographs of the **(d,e)** unmodified paper and **(f,g)** laser irradiated paper. **(h)** SEM micrograph showing a magnified view of the paper-LIG structure, evidencing its thin "veil-like" appearance. **(i)** Overview XPS spectra comparing paper and paper-LIG. **(j)** High-resolution XPS spectra of the C1s peak of the paper and paper-LIG, with the identification of the respective components. **(k)** Differentiated C KLL Auger features of paper and paper-LIG, with the corresponding D-values. (A colour version of this figure can be viewed online.)

D-values obtained from the differentiated C KLL Auger features (Fig. 1k), being equal to 10 for non-irradiated paper and 18 for paper-LIG, the latter being much closer to the values seen for sp^2-rich carbons [46]. The loss of oxygen content is also confirmed by the lowering of its atomic percentage from 41.99% in paper to 17.24% in paper-LIG. The paper-LIG is also confirmed to be conductive, possessing sheet resistances of 40–50 Ω sq^{-1}, in line with previous reports concerning paper-LIG [15]. This conductivity, coupled with the apparent porosity of paper-LIG and its defect-rich structure, make it potentially attractive as an electrochemically active material with electrocatalytic properties.

The paper-LIG electrodes were subjected to electrochemical impedance spectroscopy measurements to gain insights into the underlying electrochemical mechanisms of the porous graphene arrangement. Two different equivalent circuits were used to model the cell as schematically shown in Fig. 2. The first one, the modified Randles (MR) circuit, is commonly employed to model electrochemical response of planar electrodes and is composed of (i) an equivalent series resistance, R_s, which gathers all uncompensated resistances including contact and paper-LIG bulk resistance, (ii) a resistance R modeling possible capacitance self-discharge effects, and (iii) a constant phase element (CPE) Q, which models non-ideal capacitive behavior due to surface roughness effects. This model does not consider the porosity of the electrode material, but rather the existence of a continuous front electrode surface. On the other hand, the second one is a transmission line model as described by Bisquert [47,48], known as Bisquert open (BTO). In the BTO, only phenomena occurring at the inner pore walls are taken into account, and the base electrode region is considered inactive. R_{EL} represents the pore resistance to electrolyte diffusion and ζ the reactions occurring at the inner pore surface, constituted by a parallel combination of a resistor and a CPE. Pore depth is represented by L and dashed circuit lines represent the stepwise repetition of the $R_{EL}||\zeta$ block along the pore. Detailed information on transmission line models and simplifications/assumptions of the Bisquert open model can be found in the related original works [47,48].

It is clear from the high-frequency portion of the Bode and Nyquist plots that the electrochemical cell is characterized by relatively low internal resistances R_s, demonstrating the conductive nature of paper-LIG, in agreement with the Van der Pauw measurements that returned a sheet resistance of 40–50 Ω sq^{-1}. On the other hand, the MR circuit shows a poor agreement with the impedance spectrum at all frequency ranges as seen in the Bode plots of Fig. 2b and in the Nyquist plots of Fig. 2c. It fails to describe the incremental increase of |Z| with decreasing frequency down to 1 Hz as well as the particular evolution of the phase at higher frequencies (Fig. 2b). It also fails to explain the response in the complex plane at higher frequencies, where a straight line with approximately a unitary slope is observed (inset of Fig. 2c). These features arise from porosity effects, which are contemplated by the BTO model, which in turn denotes excellent agreement with the data at all frequencies, both in the Bode and Nyquist plots. Hence, it is clear that porosity plays a role in the electrochemical response of paper-LIG electrodes, similarly to the observed for PI-LIG [49] using the same electrolyte. Note that Fig. 2a shows a schematic representation of paper-LIG porosity as an inter-fiber arrangement, but in fact the intra-fiber porosity should actually be the porosity governing the observed impedimetric response, so that Fig. 2a is to be interpreted regarding schematization purposes only. Table S1 and Table S2 in Supplementary Material compile the fitting results of the MR and BTO models, respectively.

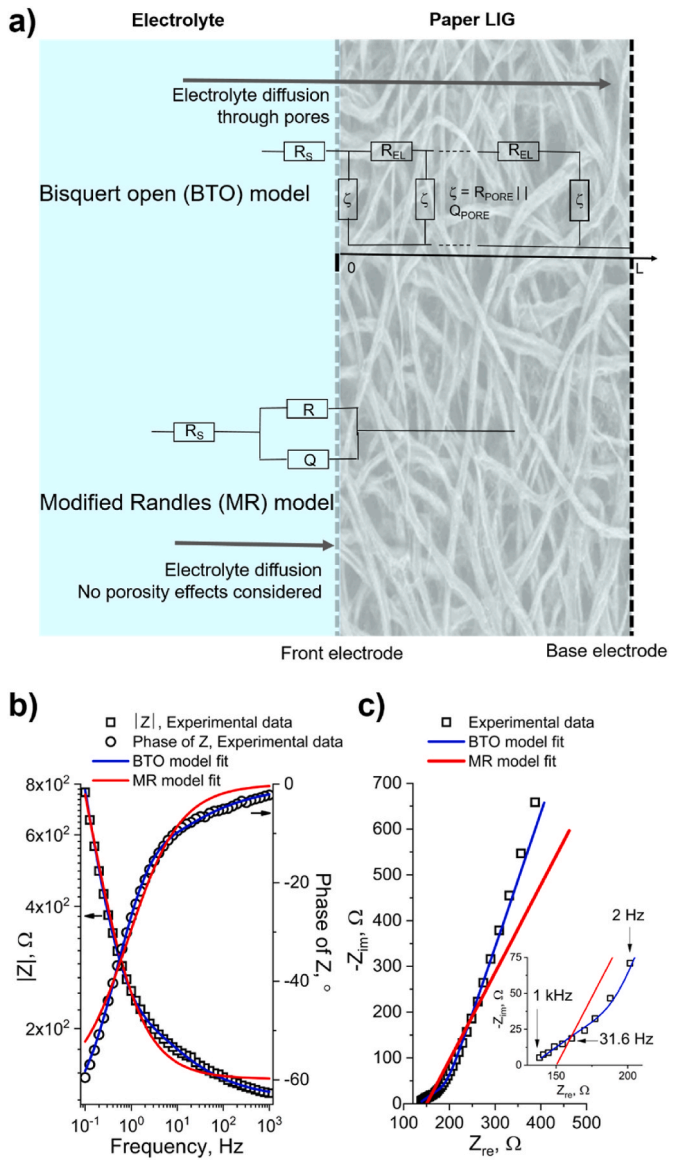

Fig. 2. EIS characterization of paper-LIG electrodes.
(a) Schematic representation of the paper-LIG-electrolyte interface and the two equivalent circuit models employed to describe the impedimetric response, which is shown via the **(b)** Bode and **(c)** Nyquist plots. Note that the number of points in the data of the inset in (c) has been reduced for clarity's sake. The electrolyte is 3.5 M KCl aqueous solution. (A colour version of this figure can be viewed online.)

The electron transfer capabilities of the paper-LIG electrodes were assessed via cyclic voltammetry analysis employing reversible, well-behaved redox pairs, $[Ru(NH_3)_6]^{2+/3+}$ and $[Fe(CN)_6]^{4-/3-}$. The usage of different redox pairs to characterize the electrochemical response is desirable, allowing probing different potential window regions, distinct charge states and reaction mechanisms at the electrode surface. The outer-sphere $[Ru(NH_3)_6]^{2+/3+}$ redox system is regarded as a standard probe for heterogeneous electron transfer (HET) analysis, permitting a general comparison among different electrodes whilst minimizing surface chemistry effects on HET, which can be exacerbated employing inner sphere redox pairs, such as $[Fe(CN)_6]^{4-/3-}$. Fig. 3a shows the cyclic voltammograms of 5 mM $[Ru(NH_3)_6]^{2+/3+}$ in PBS (pH 7.4) at varying scan rate (ν).

The voltammograms denote well-defined anodic and cathodic waves, with peak-to-peak separation (ΔE_p) falling within 120–335 mV and a half wave potential of −200 mV vs. SCE. Peak currents of both

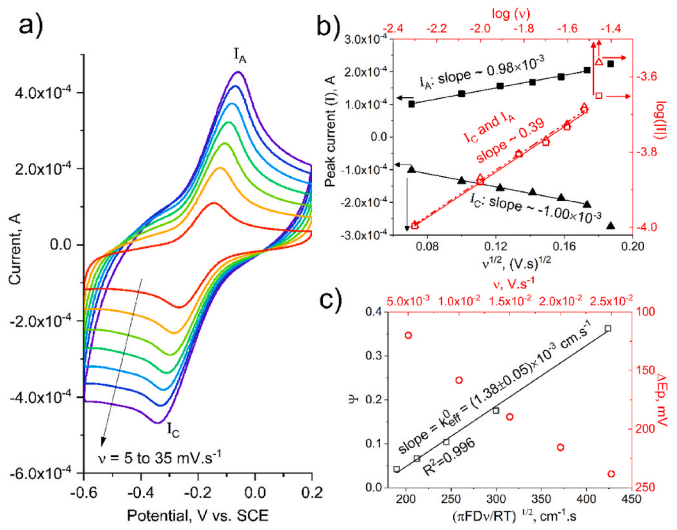

Fig. 3. CV characterization of paper-LIG electrodes using $[Ru(NH_3)_6]^{2+/3+}$ redox pair.
(a) Cyclic voltammograms at varying scan rate (from red to purple: 5, 10, 15, 20, 25, 30 and 35 mV s^{-1}) of paper-LIG electrode in PBS (pH 7.4) containing 5 mM $[Ru(NH_3)_6]^{3+}$. **(b)** Anodic and cathodic peak current versus square root of scan rate (black squares and triangles, respectively) after capacitive current subtraction, and the corresponding linear regressions (solid black lines). Logarithmic correlation plot between peak current and scan rate for the cathodic (red triangles) and anodic (red squares) branches, along with the corresponding linear regressions (dashed and solid red lines, respectively). **(c)** HET kinetic analysis within the scan rate range of 5–25 mV s^{-1}, showing ΔE_p (red circles) and kinetic parameter Ψ (black squares) obtained via Equation (1), along with the linear regression (solid black line) for estimation of effective HET standard rate constant, k^0_{eff}, via Equation (2). (A colour version of this figure can be viewed online.)

cathodic and anodic branches increase linearly with the square root of the scan rate with similar slopes (Fig. 3b), indicating that the redox reaction is limited by semi-infinite planar-diffusion of $[Ru(NH_3)_6]^{2+/3+}$ species. The log(I)-log(ν) plot of Fig. 3b denotes superimposed linearity for the anodic and cathodic branches with slopes of about 0.4. Whilst close to the theoretical value of 0.5 for a purely semi-infinite diffusion process, the observed deviations point to the presence of a competing mechanism to electron transfer. Such deviations are observed often for several electrode materials and in the present case it is most likely due to the thin layer effect [50], where small portions of electrolyte are trapped within the immediate surroundings of the electrode surface, thus influencing the process of diffusion of electroactive species. This is prone to occur in porous and intricate morphologies such as the present paper-LIG and is in accordance with the need to consider a transmission line model to properly describe the electrode's impedimetric response. Nevertheless, the present analysis indicates that the redox reaction proceeds in a quasi-reversible regime suitable for HET kinetic analysis employing the Nicholson method (Fig. 3c). The calculated effective HET standard rate constant, k^0_{eff}, is about 1.4×10^{-3} cm s^{-1}, which is nearly one order of magnitude lower than that calculated in similar experimental conditions for LIG on polyimide [16], yet comparable to several types of graphene-based electrodes reported in the literature [40,51,52].

Regarding the inner-sphere $[Fe(CN)_6]^{4-/3-}$ redox pair, the voltammograms also denote well-defined anodic and cathodic waves with half wave potential of 186 mV (Fig. S2a). The log(I)-log(ν) slopes are about 0.44 and peak currents also scale linearly with the square root of the scan rate, yet at different cathodic/anodic slopes, as seen in Fig. S2b. This indicates a higher irreversibility degree of the redox reaction. Compared to $[Ru(NH_3)_6]^{2+/3+}$, the k^0_{eff} for $[Fe(CN)_6]^{4-/3-}$ is therefore lower, 7.8×10^{-4} cm s^{-1} (Fig. S2c), a value slightly higher than the one

obtained from independently conducted measurements concerning a paper-LIG enzymatic glucose sensor [35]. This is an order of magnitude lower compared to LIG on polyimide [16] for the same redox probe in similar experimental conditions, but still comparable to other graphene-based electrodes in the literature [40,53].

All around, these results underline the appropriate structural arrangement as well as electrical and electron transfer capabilities of paper-LIG, suitable for electroanalytical purposes, further encouraging the study of non-enzymatic detection of clinically relevant analytes via direct electrooxidation/reduction, such as the case of uric acid as presented in the following sections.

3.2. Quantification of uric acid in PBS

The uric acid electrochemical oxidation on paper-LIG electrodes was evaluated employing different PBS formulations yielding different pH values, specifically pH 7.4, 6.6 and 5.6 at a constant ionic strength, up to a concentration of UA of 300 μM, close to the solubility limit of UA in water (~350 μM) [54]. Actually, in urine, UA is found at much higher concentrations, as this complex matrix contains for instance proteins and other compounds aiding to achieve a higher solubility [55,56]. Moreover, temperature, ionic strength, and pH also play an important role in the solubility of UA [54]. Uric acid is a diprotic acid that, above its acid dissociation constant ($pK_{a1} = 5.4$ and $pK_{a2} = 9.8$), appears in the form of urate ions [57], see the chemical structure in Fig. S3a.

Fig. 4a shows the DPV oxidation waves assignable to uric acid electrochemical oxidation into a diimide quininoid by transferring 2 protons and 2 electrons (see Fig. S3b). The diimide quininoid is very unstable and undergoes subsequent reactions, which follow different pathways dependent of the pH below or above the pK_a, forming for instance allantoin [58,59]. For pH 7.4 and 6.6, the DPV peaks are sharp and well-defined, whereas for pH 5.6 (close to the pK_{a1}) they tend to widen. The deformed peak shape at pH 5.6 could therefore evidence the contribution of other redox processes downstream of UA oxidation, such as the presence of intermediary subproducts of the redox reaction at pH $\leq pk_{a1}$ that have electroactivity near or superimposed to the UA [59]. A strong linear correlation ($R^2 = 0.999$) between peak current density and UA concentration exists at pH 7.4 up to 250 μM, whilst linearity is progressively lost with decreasing pH for values close to pK_{a1} (Fig. 4b), even though peak current densities and sensitivity increase with decreasing pH, as observed elsewhere [60,61]. The peak potential shifts linearly with the pH within the 5.6 to 7.4 range at a rate of −75 mV pH^{-1} for 50 μM UA (see Fig. S4). A similar behavior was found by Liu et al. [62], where a slope of −73 mV pH^{-1}, in a pH range from 4 to 8, was obtained for a wide range of UA concentrations (5–600 μM). The observed linear behavior indicates that the same reaction regime, the UA oxidation into diimide quininoid, is ruling in this pH range.

The limit of detection (LoD) for pH 7.4 is 3.97 μM, calculated via the calibration curve using the $3\sigma/S$ criterion, where σ is the standard deviation of the *y*-intercept of the analytical curve and *S* is the sensitivity equaling the slope of the analytical curve [63]. The LoD obtained for these non-enzymatic sensing units based on paper-LIG is higher compared to some enzymatic biosensors presented in the literature, including paper-based sensors, where LoD as low as 0.06 μM [64] and 0.008 μM [65] have been reported. It is also slightly higher compared to non-enzymatic LIG sensors scribed on polyimide and modified with Pt nanoparticles (0.22 μM) [66]. Nevertheless, one should keep in mind that extremely low LoD is not mandatory regarding UA detection and quantification in human urine, given the reference values usually under consideration, above 1 mM [38,67]. Indeed, the paper-LIG electrodes provide a linear range within 10–250 μM UA, which constitutes a wide and useable range suitable for analysis of dilute urine samples. For instance, using a 1:20 dilution, this means that UA quantification is possible in the range of about 200 μM to 5 mM, which covers the 1 mM–4.4 mM range taken as reference values encountered in real, non-diluted human urine [67]. Moreover, these simple, environmentally-friendly and inexpensive sensing units provide a sensitivity of 0.363 μA cm^{-2} μM^{-1} at pH 7.4, which surpasses that of some enzymatic UA sensors reported in the literature that are much more complex and costly to produce [64,68]. Compared to PI-LIG UA sensors, for which electron transfer kinetics are found to be impressive [16], sensitivities are one order of magnitude lower, 5.4 μA cm^{-2} μM^{-1} for PI-LIG [66], yet within a much narrower UA concentration range up to 20 μM and for which no measurements in biological fluids were demonstrated. Table 1 gathers several reports on non-enzymatic UA sensors based on LIG, for comparison purposes.

Reproducibility among sensing units is found to be highly dependent on the UA concentration. Relative standard deviations of the signal from quadruplicates diminish with increasing UA concentration, being above 20% for 10 and 20 μM UA and below 11% for 50 μM UA and above, for both pH 7.4 and pH 6.6, and always below 8% for pH 5.6. Moreover, the electroanalytical performance has shown no dependence on long-term

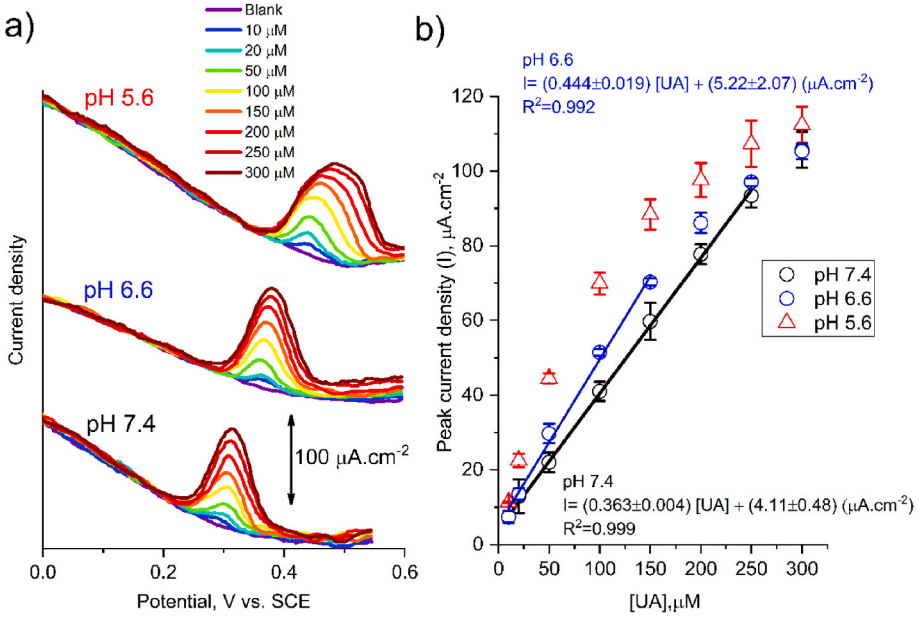

Fig. 4. Quantification of uric acid in PBS.
(a) DPV response of paper-LIG electrodes in UA-containing PBS at different pH values. Measurements at each pH are grouped and shifted in intensity for clarity. **(b)** Corresponding peak current density versus concentration of UA and linear calibration curves, where applicable. Error bars are standard deviations from independent quadruplicate measurements. (A colour version of this figure can be viewed online.)

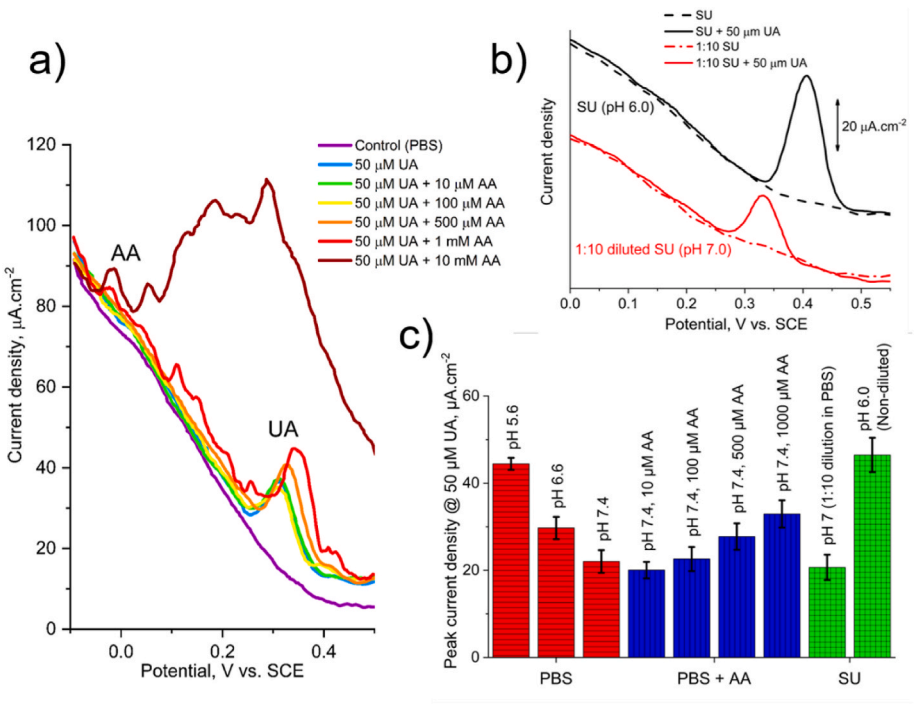

Fig. 5. Selectivity tests.
DPV scans at 50 μM UA concentration: **(a)** in PBS (pH 7.4) plus varying concentrations of AA, and **(b)** in non-diluted and 1:10 diluted synthetic urine (SU). In (b), DPV scans are grouped and shifted in intensity for clarity. **(c)** UA (50 μM) oxidation peak current densities for the previous measurements. Results for PBS at varying pH (see also Fig. 4) are also shown for comparison. Error bars are standard deviations from independent quadruplicate measurements. (A colour version of this figure can be viewed online.)

Table 1
Comparison of figures of merit determined for LIG-based biosensors for non-enzymatic detection of uric acid.

Electrode	Linear Range(s) (μM)	Sensitivity ($\mu A.\mu M^{-1}.cm^{-2}$)	LoD (μM)	Detection technique	Selectivity tests	Tested in real samples?	[Ref]
Paper-LIG	10–250	0.363	3.97	DPV	AA, DA, synthetic urine	Human urine	This work
PI-LIG	~0–20	5.4	–	DPV	–	No	[66]
PI-LIG/Pt NPs	~0–60	8.29	0.22	DPV	AA, DA	No	[66]
PI-LIG on ITO	5–100	3.1	5.0 (measured)	DPV	AA, DA	No	[69]
PI-LIG	3–40	3.50	0.74	DPV	Glucose, tyrosine, urea, DA, AA	Human sweat	[70]
PI-LIG/PBSE/Pt NPs	5–480	0.157	0.018	Amperometry	AA, lactic acid, acetaminophen	No	[71]
PI-LIG/Chitosan/Au NPs	1-30; 30–100	1.65; 0.48 ($\mu A\ \mu M^{-1}$)	0.33	DPV	AA, DA, Glucose, lactate	Human blood serum	[72]

*DA-dopamine, AA-ascorbic acid, NPs – nanoparticles, ITO – indium tin oxide, PBSE - succinimide ester.

storage up to one year, the response of the sensing units varying within the mentioned standard deviation values with no observable correlation with storage time.

3.3. *Selectivity tests – ascorbic acid, dopamine and synthetic urine*

Ascorbic acid (AA), also known as vitamin C, is a major interfering agent in clinical analysis, including urinalysis. Studies employing commercially available dipstick tests unambiguously show that the presence of AA in the urine samples severely interferes with bilirubin, nitrite, hemoglobin and glucose detection, causing false negative results [73,74]. Moreover, ascorbic acid is an electroactive compound that often interferes in electroanalytical measurements, especially with analytes for which the formal redox potential is close to that of AA, which is the case of dopamine [16,66], and of UA to a lesser extent. Ascorbic acid in urine can reach relevant levels depending on the amounts of vitamin C ingestion, mostly when ingested as supplementation [73,74]. The selectivity test against AA of the paper-LIG UA sensors in PBS (pH 7.4) is presented in Fig. 5a.

Ascorbic acid exists as a monovalent anion at physiological pH of 7.4 denominated by ascorbate [75], which can be electrochemically oxidized into dehydroascorbate (DHA) by the loss of two electrons and one proton [75]. This reaction occurs at about 0 V vs. SCE. At lower AA concentrations, the signal from this reaction is low in intensity and rather broad. In fact, it is known that AA presents lower adsorption strength on graphene-based surfaces compared to UA, namely on LIG, resulting in much lower oxidation currents for similar concentrations [16,66,76]. Both, AA and UA, at physiological pH (pI 4.2 and 5.4, respectively) are found in their anionic form favoring electrostatic repulsion with the LIG surface, namely due to carboxyl groups present on LIG structure as confirmed by XPS (Fig. 1j). Still, the fact that UA possesses some degree of aromaticity in its molecular structure, whereas AA does not, favors UA adsorption onto sp^2-rich carbon surfaces, such as paper-LIG (see Raman spectra and XPS in Fig. 1).

The UA oxidation signal is unperturbed up to 100 μM AA, with the peak current densities falling within the range as determined for 50 μM UA in PBS (pH 7.4) as shown in Fig. 5c. At 500 μM AA and above, the AA oxidation peak at 0 V becomes more defined, several additional anodic waves appear downstream of AA oxidation and the UA oxidation currents increase beyond the expected range. At 10 mM AA, the signal from UA is heavily masked by such reactions, the nature of which is complex and beyond the scope of the present paper. These results indicate

relevant interference from AA activity at 500 μM AA and above (Fig. 5c). Moreover, after measurements at high AA concentrations and after thorough stirring and washing in DI water, AA and/or DHA-related anodic peaks still appear in the DPV in pure PBS electrolyte, indicating that electrode fouling by AA and related oxidation products has occurred. Hence, the paper-LIG UA sensors suffer from interference and fouling in AA containing electrolyte solutions, yet only at abnormally high AA concentrations. Considering a 1:20 urine dilution as employed in the next section whilst measuring real human urine samples, this would correspond to a concentration of roughly 10 mM AA. Such values did not occur in the human urine collected from volunteers after ingestion of several doses of Vitamin C -containing juices [74], but do occur in the case of Vitamin C supplementation, yet at relatively low probabilities and only at high ingestion doses, above 500 mg [74]. Although out of the scope of this work, it is of note that the use of acetate buffers (pH 4) is reported elsewhere to suppress or minimize the interference of high concentrations of AA in UA detection when employing glassy carbon electrodes [60], which can be a useful strategy for paper-LIG electrodes in such situations.

In addition to AA, dopamine (DA) also constitutes a potential interferent in UA quantification due to its easy electrooxidation and formal electrode potential close to that of UA [16]. DA belongs to the family of catecholamines, constituting a neurotransmitter in several pathways in the central nervous system, with special activity in the kidneys. Normal DA levels in human urine can reach 2–3 μM in 24 h urine tests [77,78], but can be substantially increased in case of some physiological conditions and diseases, such as specific tumors [78]. As seen in Fig. S5, paper-LIG electrodes are able to separate DA and UA signals by ~150 mV and the quantification of UA is immune to abnormally high DA levels (up to 20 μM), despite some overlapping of DA and UA oxidation waves at higher DA concentrations. This is two orders of magnitude higher than the maximum (normal) levels of DA when considering 1:10 and 1:20 human urine dilutions as employed in this work.

Selectivity tests were also conducted in synthetic urine (SU) samples, the composition of which is detailed in the experimental section. As seen in Fig. 5b, despite the complex formulation of possible interferents in UA detection, none of the constituents of SU induces any measurable faradaic activity in the potential range of interest and hence no direct interference occurs, even if measuring non-dilute samples. Peak potentials closely follow a linear trend with pH at a −75 mV pH^{-1} slope for a UA concentration of 50 μM, as seen in Fig. S4. This is in line with the observed for measurements in PBS at varying pH, confirming that reaction mechanisms and kinetics are unaltered by the compounds present in SU.

3.4. Determination of uric acid in real human urine samples

Fig. 6a shows the DPVs of a paper-LIG electrode in 1:10 and 1:20 dilutions of real human urine in PBS (pH 7.4). Uric acid recoveries were tested in 1:20 diluted urine by spiking 50 and 100 μM of uric acid followed by stirring for 5 min, and the corresponding DPVs are also shown. Table 2 gathers and details all the measurements and the retrieved values of UA content in urine samples. Firstly, no signs of interfering electroactive species are discernible near the UA oxidation peak. Secondly, the electrochemically inactive species present in urine, such as proteins, have not affected the analytical performance of the electrodes (Fig. 6b) taking the calibration curve in PBS pH 7.4 as reference. Indeed, regarding the 1:20 diluted urine, the results point to a concentration of about 1.83 mM of UA in the non-diluted urine, which is consistent with the expected for urine from healthy individuals, within the ~1–4.4 mM range [67]. Furthermore, the value often taken as reference for 24 h urine tests is about 1 mM [38], yet it is to note that in this work the samples correspond to first morning urine, which tends to concentrate UA.

The average UA recoveries for spiked samples of 1:20 diluted urine are very close to 100%, demonstrating the accuracy of the paper-LIG

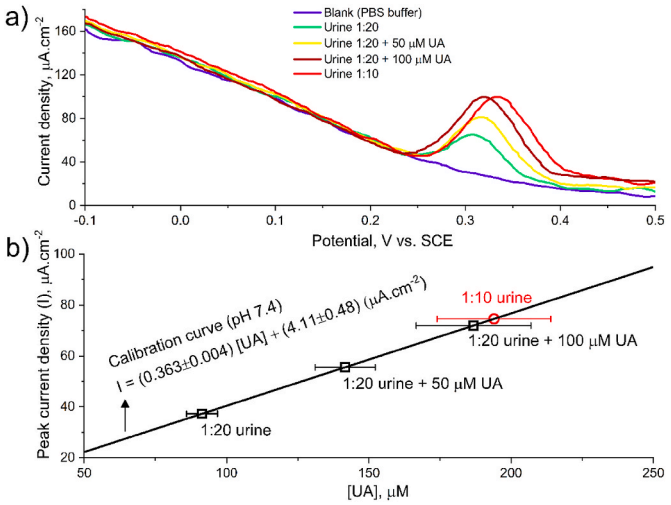

Fig. 6. Uric acid quantification in real human urine samples.
(a) DPV scans of paper-LIG electrode in diluted urine and spiked urine samples. **(b)** Determination of UA content using the calibration curve in PBS (pH 7.4). Horizontal error bars are standard deviations from quadruplicate measurements. (A colour version of this figure can be viewed online.)

Table 2
Determination of uric acid in diluted urine and spiked urine samples. Standard deviations from quadruplicate measurements are also shown.

Trial	Spiked UA concentration (μM)	Average UA content retrieved from calibration plot (μM)	Standard deviation (μM, %)	Average recovery (%)
1:20 urine	0	91.39	5.48, 5.94	–
1:20 urine + 50 μM UA	50	141.68	10.59, 7.47	100.58
1:20 urine + 100 μM UA	100	186.78	20.12, 10.77	95.39
1:10 urine	0	193.97	19.99, 10.30	–

sensing units and of the measuring methods. A dilution of 1:10 urine was also measured for comparison purposes. Results indicate a concentration of 1.94 mM of UA in non-diluted urine samples, about 106% of that found via the 1:20 diluted urine. This discrepancy is within the standard deviation of the measurements. It is notable that the pH was seen to drop from 7.3 for 1:20 diluted urine to about 7.0–7.1 for 1:10 diluted urine, causing a shift of the oxidation peak towards more positive potentials (red curve in Fig. 6a). This is in agreement with measurements in synthetic urine where a 1:10 dilution, pH 7.0, yielded statistically similar current densities compared to those in PBS (pH 7.4).

Reproducibility among different paper-LIG electrodes for measurement of real human urine is satisfactory, always below 11% relative standard deviation (n = 4), increasing with UA content.

Despite the inherent suitableness of paper-LIG to be employed as disposable sensing units due to their low cost and environmental friendliness, these electrodes are in fact reusable. Indeed, a blank baseline without any faradaic activity from UA can be easily recovered for every electrode after washing with DI water, after employing either PBS or 1:20 diluted urine in PBS (Fig. S6a). Moreover, the original UA oxidation signal could be recovered after washing with DI water

(Fig. S6b). This denotes a good stability and repeatability of the paper-LIG electrodes and shows that no severe electrode fouling has occurred. However, the DI water-washing step is necessary, given a small but relevant current intensity from oxidation of adsorbed UA obtained when measuring in pure PBS solution the unwashed electrodes that had previously been subjected to measurements in UA-containing electrolyte solutions.

4. Conclusions

Paper-LIG constitutes a suitable material for uric acid (UA) quantification in human urine. The porous graphene network formed after CO_2 laser irradiation of paper exhibits adequate electron transfer capabilities, characterized by effective heterogeneous electron transfer standard rate constants of 1.4×10^{-3} cm s^{-1} and 7.8×10^{-4} cm s^{-1} for $[Ru(NH_3)_6]^{2+/3+}$ and $[Fe(CN)_6]^{4-/3-}$ redox probes, respectively. Quantification of UA is immune to physiologically relevant concentrations of dopamine and to several interferents present in synthetic urine formulations. Ascorbic acid (AA) is shown to interfere but only at concentrations of 500 μM and above. Since the determination of UA in real human urine was performed employing 1:20 dilutions in PBS, interference with AA only starts at urinary concentrations of about 10 mM, which seldom occurs and specifically in cases of heavy vitamin C supplementation. Determination of UA in real human urine returned a concentration of c. a. 1.8–1.9 mM and recoveries from spiked samples were about 100.6% and 95.4% for 50 and 100 μM spiked UA concentrations, respectively. These results demonstrate that non-enzymatic uric acid detection is possible using considerably cheaper and more widely available materials than the previously reported commercial polymer derived LIG biosensors. With satisfactory reproducibility and repeatability upon long term storage at ambient conditions, and allowing both reusability and disposable applications, these paper-LIG sensors are a smart solution for biosensing within the contemporary paradigm focused on materials and processing sustainability.

Data availability

The raw data required to reproduce these findings are available from the authors upon request. The processed data required to reproduce these findings are available from the authors upon request.

CRediT authorship contribution statement

Bohdan Kulyk: Conceptualization, Investigation, Software, Methodology, Visualization, Writing – original draft, Writing – review & editing. **Sónia O. Pereira:** Conceptualization, Investigation, Methodology, Resources, Writing – review & editing. **António J.S. Fernandes:** Conceptualization, Investigation, Methodology, Writing – review & editing. **Elvira Fortunato:** Supervision. **Florinda M. Costa:** Conceptualization, Funding acquisition, Methodology, Supervision, Writing – review & editing. **Nuno F. Santos:** Conceptualization, Investigation, Software, Methodology, Resources, Visualization, Writing – original draft, Writing – review & editing.

Declaration of competing interest

The authors declare that they have no known competing financial interests or personal relationships that could have appeared to influence the work reported in this paper.

Acknowledgements

This work was developed within the scope of project i3N (LA/P/0037/2020, UIDB/50025/2020 and UIDP/50025/2020), financed by national funds through the Portuguese Foundation for Science and Technology/MCTES (FCT I.P.). B. Kulyk acknowledges the PhD grant SFRH/BD/141525/2018 from FCT I.P. N. F. Santos thanks i3N for the BPD Grant BPD/UI96/5177/2020. S. O. Pereira thanks i3N for the BPD Grant BPD/UI96/5808/2017. The financial support by National Funds through FCT I.P. under the NANOBIOSENSE project PTDC/NAN-MAT/28755/2017 (POCI-01-0145-FEDER-028755) is gratefully acknowledged. E. Fortunato acknowledges the ERC AdG grant 787410 from the project DIGISMART. The authors also thank Jonas Deuermeier for the XPS measurements.

Appendix A. Supplementary data

Supplementary data to this article can be found online at https://doi.org/10.1016/j.carbon.2022.06.013.

References

[1] K.S. Novoselov, A.K. Geim, S.V. Morozov, D. Jiang, Y. Zhang, S.V. Dubonos, I. V. Grigorieva, A.A. Firsov, Electric field effect in atomically thin carbon films, Science 306 (2004) 666–669, https://doi.org/10.1126/science.1102896, 80-.

[2] A.C. Ferrari, F. Bonaccorso, V. Falko, K.S. Novoselov, S. Roche, P. Bøggild, S. Borini, F. Koppens, V. Palermo, N. Pugno, J.a. Garrido, R. Sordan, A. Bianco, L. Ballerini, M. Prato, E. Lidorikis, J. Kivioja, C. Marinelli, T. Ryhänen, A. Morpurgo, J.N. Coleman, V. Nicolosi, L. Colombo, A. Fert, M. Garcia-Hernandez, A. Bachtold, G.F. Schneider, F. Guinea, C. Dekker, M. Barbone, C. Galiotis, A. Grigorenko, G. Konstantatos, A. Kis, M. Katsnelson, C.W.J. Beenakker, L. Vandersypen, A. Loiseau, V. Morandi, D. Neumaier, E. Treossi, V. Pellegrini, M. Polini, A. Tredicucci, G.M. Williams, B.H. Hong, J.H. Ahn, J.M. Kim, H. Zirath, B.J. van Wees, H. van der Zant, L. Occhipinti, A. Di Matteo, I.a. Kinloch, T. Seyller, E. Quesnel, X. Feng, K. Teo, N. Rupesinghe, P. Hakonen, S.R.T. Neil, Q. Tannock, T. Löfwander, J. Kinaret, Science and technology roadmap for graphene, related two-dimensional crystals, and hybrid systems, Nanoscale 7 (2014) 4598–4810, https://doi.org/10.1039/C4NR01600A.

[3] D. Iannazzo, A. Pistone, M. Salamò, S. Galvagno, R. Romeo, S.V. Giofré, C. Branca, G. Visalli, A. Di Pietro, Graphene quantum dots for cancer targeted drug delivery, Int. J. Pharm. 518 (2017) 185–192, https://doi.org/10.1016/j.ijpharm.2016.12.060.

[4] K. Yang, L. Feng, Z. Liu, Stimuli responsive drug delivery systems based on nano-graphene for cancer therapy, Adv. Drug Deliv. Rev. 105 (2016) 228–241, https://doi.org/10.1016/j.addr.2016.05.015.

[5] S. Kumar, K. Chatterjee, Comprehensive review on the use of graphene-based substrates for regenerative medicine and biomedical devices, ACS Appl. Mater. Interfaces 8 (2016) 26431–26457, https://doi.org/10.1021/acsami.6b09801.

[6] P. Bollella, G. Fusco, C. Tortolini, G. Sanzò, G. Favero, L. Gorton, R. Antiochia, Beyond graphene: electrochemical sensors and biosensors for biomarkers detection, Biosens. Bioelectron. 89 (2015) 152–166, https://doi.org/10.1016/j.bios.2016.03.068.

[7] M. Pumera, Graphene in biosensing, Mater. Today 14 (2011) 308–315, https://doi.org/10.1016/S1369-7021(11)70160-2.

[8] M. Coroş, S. Pruneanu, R.-I.S. Staden, Review—recent progress in the graphene-based electrochemical sensors and biosensors, J. Electrochem. Soc. 167 (2019), 037528, https://doi.org/10.1149/2.0282003JES.

[9] H.L. Poh, M. Pumera, Nanoporous carbon materials for electrochemical sensing, Chem. Asian J. 7 (2012) 412–416, https://doi.org/10.1002/asia.201100681.

[10] S.C.S. Lai, A.N. Patel, K. McKelvey, P.R. Unwin, Definitive evidence for fast electron transfer at pristine basal plane graphite from high-resolution electrochemical imaging, Angew. Chem. Int. Ed. 51 (2012) 5405–5408, https://doi.org/10.1002/anie.201200564.

[11] S.K. Krishnan, E. Singh, P. Singh, M. Meyyappan, H.S. Nalwa, A review on graphene-based nanocomposites for electrochemical and fluorescent biosensors, RSC Adv. 9 (2019) 8778–8881, https://doi.org/10.1039/C8RA09577A.

[12] J. Lin, Z. Peng, Y. Liu, F. Ruiz-Zepeda, R. Ye, E.L.G. Samuel, M.J. Yacaman, B. I. Yakobson, J.M. Tour, Laser-induced porous graphene films from commercial polymers, Nat. Commun. 5 (2014) 1–8, https://doi.org/10.1038/ncomms6714.

[13] A.F. Carvalho, B. Kulyk, A.J.S. Fernandes, E. Fortunato, F.M. Costa, A review on the applications of graphene in mechanical transduction, Adv. Mater. (2021), 2101326, https://doi.org/10.1002/adma.202101326.

[14] A.F. Carvalho, A.J.S. Fernandes, C. Leitão, J. Deuermeier, A.C. Marques, R. Martins, E. Fortunato, F.M. Costa, Laser-induced graphene strain sensors produced by ultraviolet irradiation of polyimide, Adv. Funct. Mater. 28 (2018), 1805271, https://doi.org/10.1002/adfm.201805271.

[15] B. Kulyk, B.F.R. Silva, A.F. Carvalho, S. Silvestre, A.J.S. Fernandes, R. Martins, E. Fortunato, F.M. Costa, Laser-induced graphene from paper for mechanical sensing, ACS Appl. Mater. Interfaces 13 (2021) 10210–10221, https://doi.org/10.1021/acsami.0c20270.

[16] N.F. Santos, S.O. Pereira, A. Moreira, A. V Girão, A.F. Carvalho, A.J.S. Fernandes, F.M. Costa, IR and UV laser-induced graphene: application as dopamine electrochemical sensors, Adv. Mater. Technol. 6 (2021), 2100007, https://doi.org/10.1002/admt.202100007.

[17] A.R. Cardoso, A.C. Marques, L. Santos, A.F. Carvalho, F.M. Costa, R. Martins, M.G. F. Sales, E. Fortunato, Molecularly-imprinted chloramphenicol sensor with laser-

induced graphene electrodes, Biosens. Bioelectron. 124–125 (2019) 167–175, https://doi.org/10.1016/j.bios.2018.10.015.
[18] S.O. Pereira, N.F. Santos, A.F. Carvalho, A.J.S. Fernandes, F.M. Costa, Electrochemical response of glucose oxidase adsorbed on laser-induced graphene, Nanomaterials 11 (2021), https://doi.org/10.3390/NANO11081893. Page 1893. 11 (2021) 1893.
[19] B. Kulyk, B.F.R. Silva, A.F. Carvalho, P. Barbosa, A.V. Girão, J. Deuermeier, A.J. S. Fernandes, F.M.L. Figueiredo, E. Fortunato, F.M. Costa, Laser-induced graphene from paper by ultraviolet irradiation: humidity and temperature sensors, Adv. Mater. Technol. 2101311 (2022), 2101311, https://doi.org/10.1002/admt.202101311.
[20] R. Ye, Y. Chyan, J. Zhang, Y. Li, X. Han, C. Kittrell, J.M. Tour, Laser-induced graphene formation on wood, Adv. Mater. 29 (2017), 1702211, https://doi.org/10.1002/adma.201702211.
[21] A.F. Carvalho, A.J.S. Fernandes, R. Martins, E. Fortunato, F.M. Costa, Laser-induced graphene piezoresistive sensors synthesized directly on cork insoles for gait analysis, Adv. Mater. Technol. 5 (2020), 2000630, https://doi.org/10.1002/admt.202000630.
[22] B. Kulyk, M. Matos, B.F.R. Silva, A.F. Carvalho, A.J.S. Fernandes, D.V. Evtuguin, E. Fortunato, F.M. Costa, Conversion of paper and xylan into laser-induced graphene for environmentally friendly sensors, Diam. Relat. Mater. 123 (2022), 108855, https://doi.org/10.1016/j.diamond.2022.108855.
[23] Y. Chyan, R. Ye, Y. Li, S.P. Singh, C.J. Arnusch, J.M. Tour, Laser-induced graphene by multiple lasing: toward electronics on cloth, paper, and food, ACS Nano 12 (2018) 2176–2183, https://doi.org/10.1021/acsnano.7b08539.
[24] D. Ha, Z. Fang, N.B. Zhitenev, Paper in electronic and optoelectronic devices, Adv. Electron. Mater. 4 (2018), 1700593, https://doi.org/10.1002/aelm.201700593.
[25] R. Ulucak Danish, S.U.-D. Khan, Determinants of the ecological footprint: role of renewable energy, natural resources, and urbanization, Sustain. Cities Soc. 54 (2020), 101996, https://doi.org/10.1016/j.scs.2019.101996.
[26] A.W. Martinez, S.T. Phillips, M.J. Butte, G.M. Whitesides, Patterned paper as a platform for inexpensive, low-volume, portable bioassays, Angew. Chem. Int. Ed. 46 (2007) 1318–1320, https://doi.org/10.1002/anie.200603817.
[27] M. Sajid, A.-N. Kawde, M. Daud, Designs, formats and applications of lateral flow assay: a literature review, J. Saudi Chem. Soc. 19 (2015) 689–705, https://doi.org/10.1016/j.jscs.2014.09.001.
[28] E. Carrilho, A.W. Martinez, S.T. Phillips, G.M. Whitesides, Diagnostics for the developing world: microfluidic paper-based analytical devices, Anal. Chem. 82 (2010) 3–10, https://doi.org/10.1021/ac9013989.
[29] C. Karuwan, A. Wisitsoraat, P. Chaisuwan, D. Nacapricha, A. Tuantranont, Screen-printed graphene-based electrochemical sensors for a microfluidic device, Anal. Methods 9 (2017) 3689–3695, https://doi.org/10.1039/c7ay00379j.
[30] Y. Fan, S. Shi, J. Ma, Y. Guo, A paper-based electrochemical immunosensor with reduced graphene oxide/thionine/gold nanoparticles nanocomposites modification for the detection of cancer antigen 125, Biosens, Bioelectron 135 (2019) 1–7, https://doi.org/10.1016/j.bios.2019.03.063.
[31] M. Alafeef, K. Dighe, P. Moitra, D. Pan, Rapid, ultrasensitive, and quantitative detection of SARS-CoV-2 using antisense oligonucleotides directed electrochemical biosensor chip, ACS Nano 14 (2020) 17028–17045, https://doi.org/10.1021/acsnano.0c06392.
[32] M.A. Ehsan, S.A. Khan, A. Rehman, Screen-printed graphene/carbon electrodes on paper substrates as impedance sensors for detection of coronavirus in nasopharyngeal fluid samples, Diagnostics 11 (2021) 1030, https://doi.org/10.3390/diagnostics11061030.
[33] J.G. Giuliani, T.E. Benavidez, G.M. Duran, E. Vinogradova, A. Rios, C.D. Garcia, Development and characterization of carbon based electrodes from pyrolyzed paper for biosensing applications, J. Electroanal. Chem. 765 (2016) 8–15, https://doi.org/10.1016/j.jelechem.2015.07.055.
[34] W.R. de Araujo, C.M.R. Frasson, W.A. Ameku, J.R. Silva, L. Angnes, T.R.L. C. Paixão, Single-step reagentless laser scribing fabrication of electrochemical paper-based analytical devices, Angew. Chem. Int. Ed. 56 (2017) 15113–15117, https://doi.org/10.1002/anie.201708527.
[35] T. Pinheiro, S. Silvestre, J. Coelho, A.C. Marques, R. Martins, M.G.F. Sales, E. Fortunato, Laser-induced graphene on paper toward efficient fabrication of flexible, planar electrodes for electrochemical sensing, Adv. Mater. Interfac. 2101502 (2021), 2101502, https://doi.org/10.1002/admi.202101502.
[36] Q. Wang, X. Wen, J. Kong, Recent progress on uric acid detection: a review, Crit. Rev. Anal. Chem. 50 (2020) 359–375, https://doi.org/10.1080/10408347.2019.1637711.
[37] R. El Ridi, H. Tallima, Physiological functions and pathogenic potential of uric acid: a review, J. Adv. Res. 8 (2017) 487–493, https://doi.org/10.1016/j.jare.2017.03.003.
[38] N. Sarigul, F. Korkmaz, İ. Kurultak, A new artificial urine protocol to better imitate human urine, Sci. Rep. 91 (2019) 1–11, https://doi.org/10.1038/s41598-019-56693-4, 9 (2019).
[39] A.C. Ferrari, Raman spectroscopy of graphene and graphite: disorder, electron-phonon coupling, doping and nonadiabatic effects, Solid State Commun. 143 (2007) 47–57, https://doi.org/10.1016/j.ssc.2007.03.052.
[40] M. Velický, M.A. Bissett, P.S. Toth, H.V. Patten, S.D. Worrall, A.N.J. Rodgers, E. W. Hill, I.A. Kinloch, K.S. Novoselov, T. Georgiou, L. Britnell, R.A.W. Dryfe, Electron transfer kinetics on natural crystals of MoS2 and graphite, Phys. Chem. Chem. Phys. 17 (2015) 17844–17853, https://doi.org/10.1039/c5cp02490k.
[41] D.A.C. Brownson, C.E. Banks, The Handbook of Graphene Electrochemistry, 2014, https://doi.org/10.1007/978-1-4471-6428-9.
[42] Y. Guo, D.A. Rockstraw, Physical and chemical properties of carbons synthesized from xylan, cellulose, and Kraft lignin by H3PO4 activation, Carbon N. Y. 44 (2006) 1464–1475, https://doi.org/10.1016/j.carbon.2005.12.002.
[43] M. Jagtoyen, F. Derbyshire, Activated carbons from yellow poplar and white oak by H3PO4 activation, Carbon N. Y. 36 (1998) 1085–1097, https://doi.org/10.1016/S0008-6223(98)00082-7.
[44] L. Johansson, J.M. Campbell, O.J. Rojas, Cellulose as the in situ reference for organic XPS. Why? Because it works, Surf. Interface Anal. (2020), https://doi.org/10.1002/sia.6759.
[45] M. Smith, L. Scudiero, J. Espinal, J.-S. McEwen, M. Garcia-Perez, Improving the deconvolution and interpretation of XPS spectra from chars by ab initio calculations, Carbon N. Y. 110 (2016) 155–171, https://doi.org/10.1016/j.carbon.2016.09.012.
[46] B. Lesiak, L. Kövér, J. Tóth, J. Zemek, P. Jiricek, A. Kromka, N. Rangam, C sp2/sp3 hybridisations in carbon nanomaterials – XPS and (X)AES study, Appl. Surf. Sci. 452 (2018) 223–231, https://doi.org/10.1016/j.apsusc.2018.04.269.
[47] J. Bisquert, Influence of the boundaries in the impedance of porous film electrodes, Phys. Chem. Chem. Phys. 2 (2000) 4185–4192, https://doi.org/10.1039/b001708f.
[48] J. Bisquert, Theory of the impedance of electron diffusion and recombination in a thin layer, J. Phys. Chem. B 106 (2002) 325–333, https://doi.org/10.1021/jp011941g.
[49] N.F. Santos, J. Rodrigues, S.O. Pereira, A.J.S. Fernandes, T. Monteiro, F.M. Costa, Electrochemical and photoluminescence response of laser-induced graphene/electrodeposited ZnO composites, Sci. Rep. (2021) 1–15, https://doi.org/10.1038/s41598-021-96305-8, 111. 11 (2021).
[50] I. Streeter, G.G. Wildgoose, L. Shao, R.G. Compton, Cyclic voltammetry on electrode surfaces covered with porous layers: an analysis of electron transfer kinetics at single-walled carbon nanotube modified electrodes, Sens. Actuators, B 133 (2008) 462–466, https://doi.org/10.1016/j.snb.2008.03.015.
[51] D.A.C. Brownson, P.J. Kelly, C.E. Banks, In situ electrochemical characterisation of graphene and various carbon-based electrode materials: an internal standard approach, RSC Adv. 5 (2015) 37281–37286, https://doi.org/10.1039/c5ra03049h.
[52] D.A.C. Brownson, S.A. Varey, F. Hussain, S.J. Haigh, C.E. Banks, Electrochemical properties of CVD grown pristine graphene: monolayer- vs. quasi-graphene, Nanoscale 6 (2014) 1607–1621, https://doi.org/10.1039/c3nr05643k.
[53] L. Tang, Y. Wang, Y. Li, H. Feng, J. Lu, J. Li, Preparation, structure, and electrochemical properties of reduced graphene sheet films, Adv. Funct. Mater. 19 (2009) 2782–2789, https://doi.org/10.1002/adfm.200900377.
[54] W.R. Wilcox, A. Khalaf, A. Weinberger, I. Kippen, J.R. Klinenberg, Solubility of uric acid and monosodium urate, Med. Biol. Eng. 10 (1972) 522–531, https://doi.org/10.1007/BF02474201, 1972 104.
[55] I. Kippen, J.R. Klinenberg, A. Weinberger, W.R. Wilcox, Factors affecting urate solubility in vitro, Ann. Rheum. Dis. 33 (1974) 313–317, https://doi.org/10.1136/ARD.33.4.313.
[56] H. Iwata, S. Nishio, M. Yokoyama, A. Matsumoto, M. Takeuchi, Solubility of uric acid and supersaturation of monosodium urate: why is uric acid so highly soluble in urine? J. Urol. 142 (1989) 1095–1098, https://doi.org/10.1016/S0022-5347(17)39003-1.
[57] D.P. Chong, Theoretical study of uric acid and its ions in aqueous solution, J. Theor. Comput. Sci. 1 (2016), https://doi.org/10.4172/2376-130X.1000104.
[58] D. Lakshmi, M.J. Whitcombe, F. Davis, P.S. Sharma, B.B. Prasad, Electrochemical detection of uric acid in mixed and clinical samples: a review, Electroanalysis 23 (2011) 305–320, https://doi.org/10.1002/ELAN.201000525.
[59] R.N. Goyal, A. Brajter-Toth, G. Dryhurst, Futher insights into the electrochemical oxidation of uric acid, J. Electroanal. Chem. Interfacial Electrochem. 131 (1982) 181–202, https://doi.org/10.1016/0022-0728(82)87070-8.
[60] S.A. John, Simultaneous determination of uric acid and ascorbic acid using glassy carbon electrodes in acetate buffer solution, J. Electroanal. Chem. 579 (2005) 249–256, https://doi.org/10.1016/J.JELECHEM.2005.02.012.
[61] YaoToshio, TaniguchiYoichi, WasaTamotsu, MushaSoichiro, Anodic Voltammetry and its Analytical Application to the Detection and Simultaneous Determination of Hypoxanthine, Xanthine, and Uric Acid, Http://Dx.Doi.Org/10.1246/Bcsj.51.2937. 51 (2006) 2937–2941. doi:10.1246/BCSJ.51.2937.
[62] J. Liu, W. Lu, L. Zhang, J. Yang, Z.P. Yao, Y. He, Y. Li, Integrated hand-held electrochemical sensor for multicomponent detection in urine, Biosens. Bioelectron. 193 (2021), 113534, https://doi.org/10.1016/J.BIOS.2021.113534.
[63] A. Shrivastava, V. Gupta, Methods for the determination of limit of detection and limit of quantitation of the analytical methods, Chronicles Young Sci. 2 (2011) 21, https://doi.org/10.4103/2229-5186.79345.
[64] Q. Yan, N. Zhi, L. Yang, G. Xu, Q. Feng, Q. Zhang, S. Sun, A highly sensitive uric acid electrochemical biosensor based on a nano-cube cuprous oxide/ferrocene/uricase modified glassy carbon electrode, Sci. Rep. 10 (2020), https://doi.org/10.1038/S41598-020-67394-8.
[65] F.H. Cincotto, E.L. Fava, F.C. Moraes, O. Fatibello-Filho, R.C. Faria, A new disposable microfluidic electrochemical paper-based device for the simultaneous determination of clinical biomarkers, Talanta 195 (2019) 62–68, https://doi.org/10.1016/j.talanta.2018.11.022.
[66] P. Nayak, N. Kurra, C. Xia, H.N. Alshareef, Highly efficient laser scribed graphene electrodes for on-chip electrochemical sensing applications, Adv. Electron. Mater. 2 (2016), https://doi.org/10.1002/aelm.201600185.
[67] L.A. Pachla, D.L. Reynolds, P.T. Kissinger, Analytical methods for determining ascorbic acid in biological samples, food products, and pharmaceuticals, J. Assoc. Off. Anal. Chem. 68 (1985) 1–12.

[68] S. Verma, J. Choudhary, K.P. Singh, P. Chandra, S.P. Singh, Uricase grafted nanoconducting matrix based electrochemical biosensor for ultrafast uric acid detection in human serum samples, Int. J. Biol. Macromol. 130 (2019) 333–341, https://doi.org/10.1016/j.ijbiomac.2019.02.121.

[69] Q. Hong, L. Yang, L. Ge, Z. Liu, F. Li, Direct-laser-writing of three-dimensional porous graphene frameworks on indium-tin oxide for sensitive electrochemical biosensing, Analyst 143 (2018) 3327–3334, https://doi.org/10.1039/c8an00888d.

[70] Y. Yang, Y. Song, X. Bo, J. Min, O.S. Pak, L. Zhu, M. Wang, J. Tu, A. Kogan, H. Zhang, T.K. Hsiai, Z. Li, W. Gao, A laser-engraved wearable sensor for sensitive detection of uric acid and tyrosine in sweat, Nat. Biotechnol. 38 (2020) 217–224, https://doi.org/10.1038/s41587-019-0321-x.

[71] M. Faruk Hossain, G. Slaughter, Flexible electrochemical uric acid and glucose biosensor, Bioelectrochemistry 141 (2021), 107870, https://doi.org/10.1016/J.BIOELECHEM.2021.107870.

[72] K. Samoson, A. Soleh, K. Saisahas, K. Promsuwan, J. Saichanapan, P. Kanatharana, P. Thavarungkul, K.H. Chang, A.F. Lim Abdullah, K. Tayayuth, W. Limbut, Facile fabrication of a flexible laser induced gold nanoparticle/chitosan/porous graphene electrode for uric acid detection, Talanta 243 (2022), 123319, https://doi.org/10.1016/J.TALANTA.2022.123319.

[73] A. Unic, N. Nikolac Gabaj, M. Miler, J. Culej, A. Lisac, A. Horvat, N. Vrkic, Ascorbic acid—a black hole of urine chemistry screening, J. Clin. Lab. Anal. 32 (2018), https://doi.org/10.1002/JCLA.22390.

[74] M.L. Brigden, D. Edgell, M. McPherson, A. Leadbeater, G. Hoag, High incidence of significant urinary ascorbic acid concentrations in a west coast population–implications for routine urinalysis, Clin. Chem. 38 (1992) 426–431.

[75] G. V. Rebec, From Interferant Anion to Neuromodulator: Ascorbate Oxidizes its Way to Respectability, Electrochem. Methods Neurosci. (2007). https://www.ncbi.nlm.nih.gov/books/NBK2569/(accessed September 10, 2021).

[76] F. Gao, X. Cai, X. Wang, C. Gao, S. Liu, F. Gao, Q. Wang, Highly sensitive and selective detection of dopamine in the presence of ascorbic acid at graphene oxide modified electrode, Sens. Actuators, B 186 (2013) 380–387, https://doi.org/10.1016/j.snb.2013.06.020.

[77] Y.C. Kudva, A.M. Sawka, W.F. Young, The laboratory diagnosis of adrenal pheochromocytoma: the mayo clinic experience, J. Clin. Endocrinol. Metab. 88 (2003) 4533–4539, https://doi.org/10.1210/JC.2003-030720.

[78] J.W. Yi, E.M. Oh, K.E. Lee, J.Y. Choi, D.H. Koo, K.J. Kim, K.C. Jung, S.Y. Kim, Y. K. Youn, An exclusively dopamine secreting paraganglioma in the retroperitoneum: a first clinical case in Korea, J. Korean Surg. Soc. 82 (2012) 389–393, https://doi.org/10.4174/JKSS.2012.82.6.389.